

# $\Omega$ -Net: Fully Automatic, Multi-View Cardiac MR Detection, Orientation, and Segmentation with Deep Neural Networks

Davis M. Vigneault<sup>a,b,c,\*</sup>, Weidi Xie<sup>a,\*</sup>, Carolyn Y. Ho<sup>d</sup>, David A. Bluemke<sup>e</sup>, J. Alison Noble<sup>a</sup>

<sup>a</sup>*Institute of Biomedical Engineering, Department of Engineering, University of Oxford*

<sup>b</sup>*Department of Radiology and Imaging Sciences, Clinical Center, National Institutes of Health*

<sup>c</sup>*Tufts University School of Medicine, Sackler School of Graduate Biomedical Sciences*

<sup>d</sup>*Cardiovascular Division, Brigham and Women's Hospital*

<sup>e</sup>*University of Wisconsin-Madison, School of Medicine and Public Health*

## Abstract

Pixelwise segmentation of the left ventricular (LV) myocardium and the four cardiac chambers in 2-D steady state free precession (SSFP) cine sequences is an essential preprocessing step for a wide range of analyses. Variability in contrast, appearance, orientation, and placement of the heart between patients, clinical views, scanners, and protocols makes fully automatic semantic segmentation a notoriously difficult problem. Here, we present  $\Omega$ -Net (Omega-Net): a novel convolutional neural network (CNN) architecture for simultaneous detection, transformation into a canonical orientation, and semantic segmentation. First, a coarse-grained segmentation is performed on the input image; second, the features learned during this coarse-grained segmentation are used to predict the parameters needed to transform the input image into a canonical orientation; and third, a fine-grained segmentation is performed on the transformed image. In this work,  $\Omega$ -Nets of varying depths were trained to detect five foreground classes in any of three clinical views (short axis, SA; four-chamber, 4C; two-chamber, 2C), without prior knowledge of the view being segmented. This constitutes a substantially more challenging problem compared with prior work. The architecture was trained on a cohort of patients with hypertrophic cardiomyopathy (HCM,  $N = 42$ ) and healthy control subjects ( $N = 21$ ). Network performance as measured by weighted foreground intersection-over-union (IoU) was substantially improved in the best-performing  $\Omega$ -Net compared with U-Net segmentation without detection or orientation (0.858 vs 0.834). We believe this architecture represents a substantive advancement over prior approaches, with implications for biomedical image segmentation more generally.

**Keywords:** cardiac magnetic resonance, semantic segmentation, deep convolutional neural networks, spatial transformer networks

**2010 MSC:** 00-01, 99-00

## 1. Introduction

Pixelwise segmentation of the left ventricular (LV) myocardium and the four cardiac chambers in 2-D steady state free precession (SSFP) cine sequences is an essential preprocessing step for volume estimation (e.g., ejection fraction, stroke volume, and cardiac output); morphological characterization (e.g., myocardial mass, regional wall thickness and thickening, and eccentricity); and strain analysis (Peng et al., 2016). However, automatic cardiac segmentation remains a notoriously difficult problem, given:

- Biological variability in heart size, orientation in the thorax, and morphology (both in healthy subjects and in the context of disease).

- Variability in contrast and image appearance with different scanners, protocols, and clinical planes.
- Interference of endocardial trabeculation and papillary muscles.
- Poorly defined borders between the ventricles and the atria, as well as between the chambers and the vasculature.

Three broad approaches have been employed to address this complexity. First, the scope of the problem can be restricted, i.e., to segmentation of the LV myocardium and bloodpool in the SA view only. Second, user interaction can be used to provide a sensible initialization, supply anatomical landmarks, or correct errors. Third, prior knowledge of cardiac anatomy may be incorporated into model-based approaches. Clearly, none of these approaches is ideal: the first limiting the information which can be gleaned from the algorithm; the second being labor-

\*These authors contributed equally to this work.

Email address: [davis.vigneault@gmail.com](mailto:davis.vigneault@gmail.com) (Davis M. Vigneault)

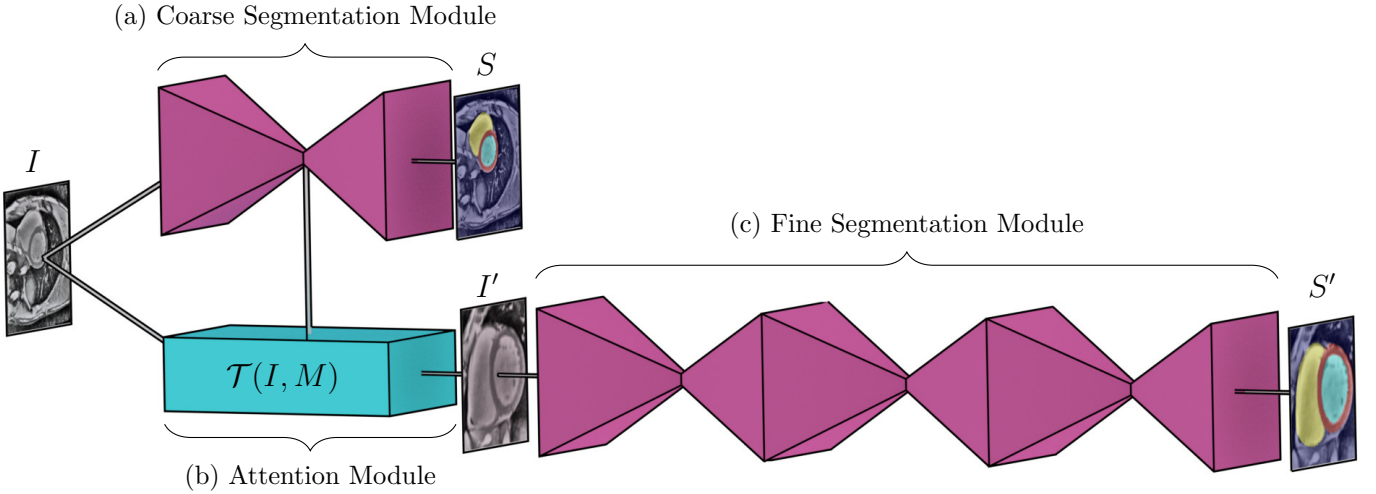


Figure 1: Overview of the ohm-net architecture. (a) The initial, unoriented SSFP image  $I$  is fed into a U-Net module, producing a coarse segmentation  $\S$ . (b) The features from the central (most downsampled) layers of this U-Net are used by the attention module to predict the parameters  $M$  of a rigid, affine transformation and transform the input image into a canonical orientation,  $I' = \mathcal{T}(I, M)$ . (c) This transformed image is fed into a stacked hourglass module to obtain a fine-grained segmentation in the canonical orientation  $S'$ . Note that, all modules shown are trained in an end-to-end way from scratch.

intensive for the clinician; and the third requiring careful construction of algorithmic constraints.

Recently, deep convolutional neural networks (CNNs) have been used to great effect both in image classification (Krizhevsky et al., 2012; Simonyan and Zisserman, 2014), and segmentation (Long et al., 2015; Noh et al., 2015; Yu and Koltun, 2016), including recently state-of-the-art performance in biomedical image analysis (Ronneberger et al., 2015; Xie et al., 2015). CNN segmentation of short axis CMR has been applied to the LV blood-pool (Tan et al., 2016; Poudel et al., 2016; Tan et al., 2017), the RV blood-pool (Luo et al., 2016), and both simultaneously (Tran, 2016; Lieman-Sifry et al., 2017; Vigneault et al., 2017). In each of these methods, either detection and segmentation was performed separately (Tan et al., 2016; Poudel et al., 2016; Tan et al., 2017; Luo et al., 2016), or detection was assumed as a component of image preprocessing (Tran (2016); Lieman-Sifry et al. (2017); Vigneault et al. (2017)). Neither end-to-end detection and segmentation nor transformation into a canonical orientation prior to segmentation has been described.

In this paper, we propose the  $\Omega$ -Net (Omega-Net), a novel CNN architecture trained end-to-end to tackle three important tasks: detection, transformation into a canonical orientation, and segmentation (Fig. 1). For simplicity, we use the U-Net as the fundamental component of the coarse- and fine-grained segmentation modules (Ronneberger et al., 2015), though more advanced networks such as Res-Net (He et al., 2016) could be substituted in the future. Inspired by the spatial transformer network (Jaderberg et al., 2015), we designed a fully differentiable architecture that achieves detection and transformation into a canonical orientation simultaneously. The trans-

formed image is then fed into a fine-grained segmentation module, which resembles the stacked hourglass architecture (Newell et al., 2016).

We demonstrate that the  $\Omega$ -Net is capable of the fully automatic segmentation of five foreground classes (LV myocardium, the left and right atria, and the left and right ventricles) in three orthogonal clinical planes (short axis, SA; four-chamber, 4C; and two-chamber, 2C), with simultaneous rigid transformation of the input into a canonical orientation (defined separately for each view, Fig. 2). Moreover, the network is trained on a multi-center population of patients with hypertrophic cardiomyopathy (HCM), which increases the complexity of the problem due to the highly variable appearance of the LV in these patients. As a result, network performance as measured by weighted foreground intersection-over-union (IoU) was substantially improved in the best-performing  $\Omega$ -Net compared with U-Net segmentation without detection and orientation alignment (0.858 vs 0.834).

## 2. Methods

Biomedical image segmentation is more efficiently accomplished if structures of interest have first been detected and transformed into a canonical orientation. In the context of CMR, the canonical orientation is defined separately for each clinical plane (Fig. 2). We propose a coarse-to-fine strategy for segmentation of cardiac SSFP images in an end-to-end differentiable CNN framework, allowing for the detection, alignment and segmentation tasks to be codependent. Our model consists of three stages. First, the full-resolution, untransformed input image  $I$  undergoes coarse-grained segmentation using a U-Net module (§2.1).

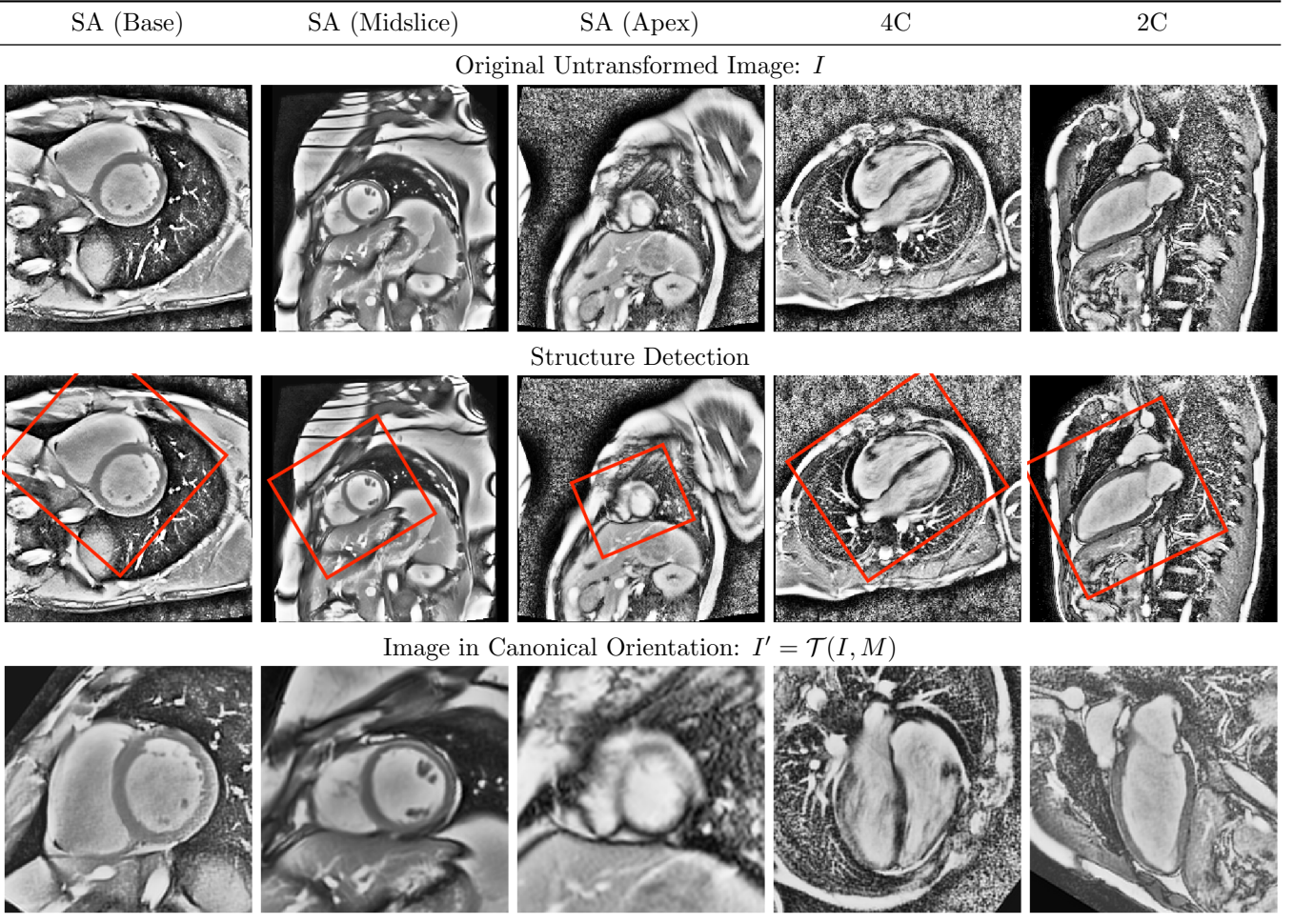


Figure 2: Orthogonal clinical views in canonical orientation. Representative short axis (SA), four-chamber (4C), and two-chamber (2C) images are shown as acquired (top), and having undergone rigid, affine transformation into a canonical orientation (bottom). Consistent with common clinical practice, the heart is rotated such that in the SA views, the right ventricle appears on the (radiological) right side of the image, whereas in the 4C and 2C views, the long axis of the left ventricle is oriented vertically. The heart is also centered and scaled to fill 90% of the image. Note the heterogeneity in size, orientation, and appearance of the heart in the untransformed images, which contributes to the difficulty of segmentation.

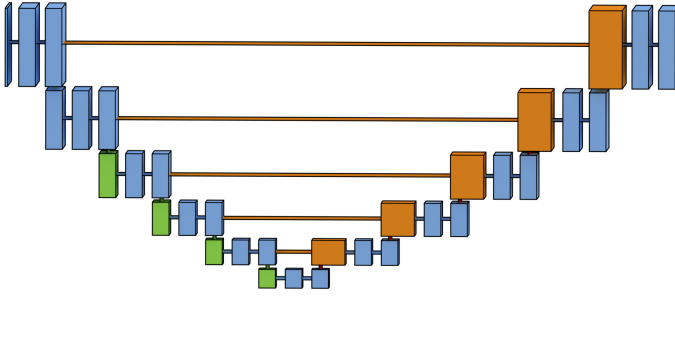


Figure 3: U-Net module. The input image is of size  $256 \times 256 \times N$ , where  $N$  is the number of channels (1 for all networks). Each blue and orange box corresponds to a multilingual feature map (orange indicates the result of a copy).

Second, the central (most downsampled) features of the aforementioned U-Net module are used to predict a rigid, affine matrix  $M$  capable of transforming  $I$  into a canonical orientation  $I' = \mathcal{T}(I, M)$  (§2.2). Third, the transformed image  $I'$  is segmented using a stacked hourglass module (§2.3). In the following subsections, each component of the network is discussed in detail. In terms of notation, a superposed chevron (e.g.,  $\hat{x}$ ) indicates ground truth, and a superscript tick (e.g.,  $x'$ ) indicates that the quantity pertains to the transformed data.

### 2.1. Coarse-grained segmentation (U-Net) module

The proposed network makes use of the U-Net module (Fig. 3), a type of deep convolutional neural network which has performed well in biomedical segmentation tasks (Long et al., 2015; Ronneberger et al., 2015; Xie et al., 2015). The U-Net architecture consists of a down-sampling path (left) followed by an up-sampling path (right) to restore the original spatial resolution. The downampling path resembles the canonical classification CNN (Krizhevsky et al., 2012; Simonyan and Zisserman, 2014), with two  $3 \times 3$  convolutions, a rectified linear unit (ReLU) activation, and a  $2 \times 2$  max pooling step repeatedly applied to the input image and feature maps. In the up-sampling path, the reduction in spatial resolution is “undone” by performing  $2 \times 2$  up-sampling, ReLU activation, and  $3 \times 3$  convolution, eventually mapping the intermediate feature representation back to the original resolution. To provide accurate boundary localization, skip connections are used, where feature representations from the down-sampling path are concatenated with feature maps of the same resolution in the up-sampling path. Batch normalization (Ioffe and Szegedy, 2015), which has been shown to counteract gradient vanishing and to lead to better convergence, was performed between each pair of convolution and ReLU activation layers. The loss  $L_{SU}$  for the U-Net module is the categorical cross entropy between the output of the softmax layer,  $P$ , and the ground truth segmentation,  $\hat{S}$ ,

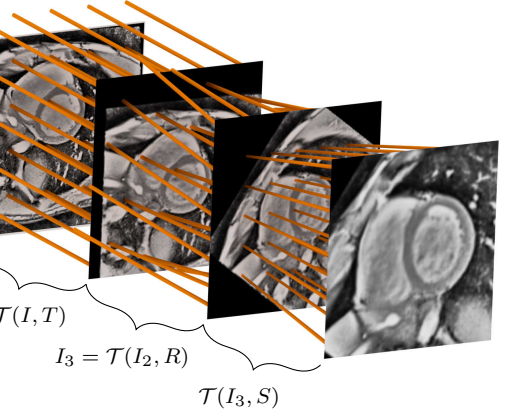


Figure 4: Spatial transformer network module. Note that in the actual implementation, all transformations are performed relative to the input image  $I$  (i.e.,  $\mathcal{T}(I, T)$ ,  $\mathcal{T}(I, RT)$ , and  $\mathcal{T}(I, SRT)$ ); for clarity, the transformations have been presented here as successive steps.

tion,  $\hat{S}$ ,

$$L_{SU} = -\frac{1}{HW} \sum_{\forall h,w} \mathcal{H}(P_{h,w}, \hat{S}_{h,w}), \quad (1)$$

where

$$\mathcal{H}(x, \hat{x}) = -\hat{x} \log(x) + (1 - \hat{x}) \log(1 - x). \quad (2)$$

### 2.2. Attention module

The spatial transformer network (STN) was originally proposed as a general layer for classification tasks requiring spatial invariance for high performance. The STN module itself consists of three submodules, namely: a localization network (LocNet), which predicts a rigid, affine transformation matrix,  $M$ ; a grid generator, which implements the transform,  $\mathcal{T}$ ; and a sampler, which implements the interpolation.

In (Jaderberg et al., 2015), the STN was allowed to learn whichever transformation parameters best aid the classification task; no ground truth transformation was specified, and the predicted transformation matrix was used to transform the intermediate *feature maps*. By contrast, in our application we are specifically interested in learning to transform the *input image* into the standard clinical orientation, as a precursor to semantic segmentation.

#### 2.2.1. Localization network (LocNet)

Intuitively, a human expert is able to provide translation, rotation, and scaling information given a rough segmentation of the heart. Based on this assumption, we branch out a small localization network (LocNet) from the layer immediately following the final max pooling step of the U-Net in order to predict the transformation parameters (Fig. 4). As we have restricted our transform to be

rigid and affine, the affine matrix was decomposed into three separate matrices:

$$M = SRT,$$

where  $T$  is the translation matrix:

$$T = \begin{bmatrix} 1 & 0 & t_x \\ 0 & 1 & t_y \\ 0 & 0 & 1 \end{bmatrix};$$

$R$  is the (counterclockwise) rotation matrix:

$$R = \begin{bmatrix} \cos(\theta) & -\sin(\theta) & 0 \\ \sin(\theta) & \cos(\theta) & 0 \\ 0 & 0 & 1 \end{bmatrix};$$

and  $S$  is the (uniform) scaling matrix:

$$S = \begin{bmatrix} s & 0 & 0 \\ 0 & s & 0 \\ 0 & 0 & 1 \end{bmatrix}.$$

Note that the images are defined on a normalized coordinate space  $\{x, y\} \in [-1, +1]$ , such that rotation and scaling occur relative to the image center.

In practice, the LocNet learns to predict only the relevant parameters,  $\mathbf{m} = [t_x \ t_y \ \theta \ s]^\top$ . During training, we explicitly provide the ground-truth transformation parameters  $\hat{\mathbf{m}} = [\hat{t}_x \ \hat{t}_y \ \hat{\theta} \ \hat{s}]$ , minimizing two types of losses, which we term *matrix losses* and *image losses*.

The matrix losses are regression losses between the ground truth and predicted parameters ( $L_{t_x}, L_{t_y}, L_\theta, L_s$ ). For scaling and translation, mean squared error (MSE) was used:

$$L_{t_x} = \frac{1}{2}(t_x - \hat{t}_x)^2, \quad (3)$$

$$L_{t_y} = \frac{1}{2}(t_y - \hat{t}_y)^2, \text{ and} \quad (4)$$

$$L_s = \frac{1}{2}(s - \hat{s})^2. \quad (5)$$

Naïve MSE is an inappropriate loss for regressing on  $\theta$  given its periodicity; this can be understood intuitively by considering ground truth and predicted rotations of  $\hat{\theta} = +\pi$  and  $\theta = -\pi$ , which yield a high MSE in spite of being synonymous. For this reason, we introduce a wrapped phase loss, mean squared wrapped error (MSWE, Fig. 5), where  $\theta - \hat{\theta}$  is wrapped into the range  $[-\pi, \pi)$  prior to calculating the standard MSE,

$$L_\theta = \frac{1}{2} \left( \mathcal{W}(\theta - \hat{\theta}) \right)^2, \quad (6)$$

and the wrapping operator  $\mathcal{W}$  is defined as

$$\mathcal{W}(\cdot) = \mod(\cdot + \pi, 2\pi) - \pi.$$

Training the attention module based on these losses alone caused the network to overfit the training data somewhat. For this reason, we additionally regularized based

on the MSE between the input image after translation, rotation, and scaling with the ground truth ( $\hat{\mathbf{m}}$ ) and predicted ( $\mathbf{m}$ ) transformation parameters:

$$L_{I_t} = \frac{1}{2}(\mathcal{T}(I, T) - \mathcal{T}(I, \hat{T}))^2, \quad (7)$$

$$L_{I_\theta} = \frac{1}{2}(\mathcal{T}(I, RT) - \mathcal{T}(I, \hat{R}\hat{T}))^2, \text{ and} \quad (8)$$

$$L_{I_s} = \frac{1}{2}(\mathcal{T}(I, SRT) - \mathcal{T}(I, \hat{S}\hat{R}\hat{T}))^2. \quad (9)$$

### 2.2.2. Grid generation and sampling

Generically, a 2-D “grid generator” takes a (typically uniform) sampling of points  $G \in \mathbb{R}^{2 \times H' \times W'}$  and transforms them according to the parameters predicted by a LocNet. In our application, we created three such grids, each of equal dimension to the input ( $H' = W' = 256$ ) and uniformly spaced over the extent of the image ( $x \in [-1, 1]$ ,  $y \in [-1, 1]$ ); these grids were then transformed by the matrices  $T$ ,  $RT$ , and  $SRT$  (predicted by the LocNet) to determine which points to sample from the input image.

The “sampler” takes the input image  $I \in \mathbb{R}^{H \times W \times C}$  and the transformed grid  $G'$  as arguments, and produces a resampled image  $I' \in \mathbb{R}^{H' \times W' \times C}$ . For each channel  $c \in [1 \dots C]$ , the output  $I'_{h', w', c}$  at the location  $(h', w')$  is a weighted sum of the input values  $I_{h, w, c}$  in the neighborhood of location  $(G'_{1, h', y'}, G'_{2, h', w'})$ ,

$$I'_{h', w', c} = \sum_{h=1}^{H-1} \sum_{w=1}^{W-1} I_{h, w, c} \cdot \max(0, 1 - |\alpha_v G'_{1, h', w'} + \beta_v - h|) \cdot \max(0, 1 - |\alpha_u G'_{2, h', w'} + \beta_u - w|),$$

where

$$\begin{aligned} \alpha_v &= +\frac{H-1}{2}, \\ \beta_v &= -\frac{H+1}{2}, \\ \alpha_u &= +\frac{W-1}{2}, \text{ and} \\ \beta_u &= -\frac{W+1}{2}. \end{aligned}$$

Every step here is differentiable (either a gradient or sub-gradient is defined), such that the model can be trained end-to-end.

### 2.3. Fine-grained segmentation (stacked hourglass) module

The output of the attention module, having been transformed into a canonical orientation, is then input into a stacked hourglass architecture. The hourglass consisted of  $D = [1 \dots 3]$  U-Net modules in series with one another, each producing a segmentation  $S_{H, d}$ , where  $d \in [1 \dots D]$ .

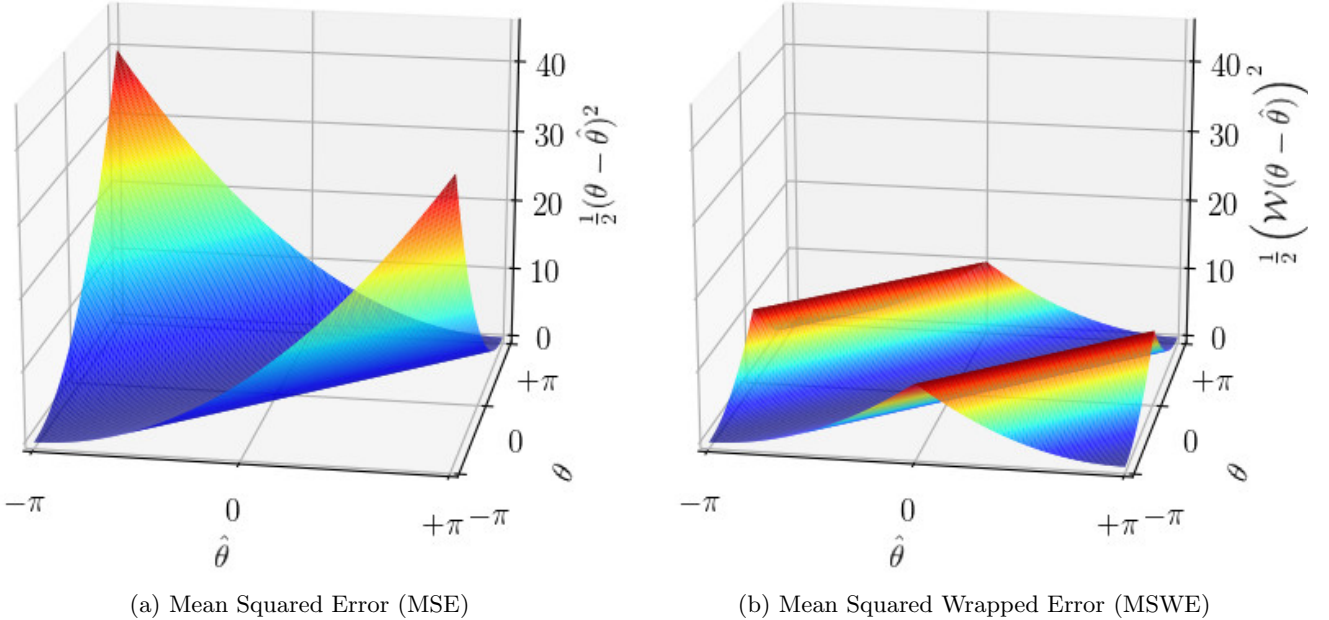


Figure 5: Mean squared error (MSE) vs mean squared wrapped error (MSWE).

With reference to Eqn. (2), the categorical cross-entropy between the softmax output of the hourglass at depth  $d$ ,  $P_{h,w}^{H,d}$  and the (transformed) ground truth  $\hat{S}'$  segmentations is calculated,

$$L_{S_{H,d}} = -\frac{1}{HW} \sum_{\forall h,w} \mathcal{H}(P_{h,w}^{H,d} \hat{S}'_{h,w}). \quad (10)$$

### 2.3.1. Summary

To summarize, we train the  $\Omega$ -Net with one loss from the coarse-grained segmentation module, eq. (1); four matrix losses, eqs. (3) to (6), and three image losses, eqs. (7) to (9), from the attention module; and between one and three losses from the fine-grained segmentation module, eq. (10). Therefore, the overall loss function may be written:

$$\begin{aligned} L_{\Omega} = & \alpha_1 L_{S_U} \\ & + \alpha_2 (L_{t_x} + L_{t_y} + L_{\theta} + L_s) \\ & + \alpha_3 (L_{I_t} + L_{I_{\theta}} + L_{I_s}) \\ & + \alpha_4 \sum_{d=1}^D L_{S_{H,d}}, \end{aligned}$$

where  $\alpha_1 = 100.0$ ,  $\alpha_2 = 100.0$ ,  $\alpha_3 = 0.1$ , and  $\alpha_4 = 1.0$ . The architectures tested are summarized in Table 1.

## 3. Experiments

### 3.1. Data preparation

The data set consisted of 63 subjects: 42 patients with overt hypertrophic cardiomyopathy (HCM) and 21 healthy

control subjects. CMR was performed with a standardized protocol at 10 centers from 2009 to 2011. Nine centers used 1.5-T magnets, and one used a 3-T magnet. Where available, three SA (basal, equatorial, and apical), one 4C, and one 2C SSFP cine series were obtained.

The LV myocardium, and all four cardiac chambers were manually segmented in the SA, 4C, and 2C views (noting that not all classes are visible in the SA and 2C views). The papillary muscles and the trabeculation of the LV and RV were excluded from the myocardium.

Each volume was cropped or padded as appropriate to  $256 \times 256$  pixels in the spatial dimensions, and varied from 20 to 50 frames in the time dimension. Nonuniform background illumination was corrected by dividing by an estimated illumination field, and background corrected images were histogram equalized. Each individual image was normalized to zero mean and unit standard deviation before being input into the CNN.

### 3.2. Training and cross-validation

For cross-validation, the subjects were partitioned into three folds of approximately equal size (4477, 4750, and 4625 images, respectively) such that the images from any one subject were present in one fold only. Each of the four architectures (Table 1) were trained on all three combinations of two folds and tested on the remaining fold.

The networks were initialized with orthogonal weights Saxe et al. (2014), and were optimized using Adam (Kingma and Ba, 2015) by minimizing categorical cross-entropy. The learning rate was initialized to 0.001 and decayed by 0.1 every 26 epochs. To avoid over-fitting, data augmentation (translations and scaling  $\pm 0.15\%$  of the image width; rotations  $\pm 0.15^\circ$ ) and a weight decay of  $10^{-4}$  was used.

Name	UNet 0	UNet 1	UNet 2	UNet 3	Millions of Parameters
Network A	128	—	—	—	7.0
Network B	64	64	—	—	3.5
Network C	64	64	64	—	4.5
Network D	64	64	64	64	5.5

Table 1: CNN architecture variants considered.

### 3.3. Measure of performance

Weighted foreground intersection-over-union (IoU) was calculated imagewise between the prediction and manual segmentations. For a binary image (one foreground class, one background class), IoU (also known as the Jaccard index) is defined for the ground truth and predicted images  $I_T$  and  $I_P$  as

$$IoU(I_T, I_P) = \frac{|I_T \cap I_P|}{|I_T \cup I_P|}, \quad (11)$$

noting that a small positive number should be added to the denominator in a practical implementation to avoid division by zero. To extend this concept to multiclass segmentation, IoU was calculated separately for each foreground class. A weighted sum of these five IoU values was then calculated, where the weights were given by the ratio between the relevant foreground class and the union of all foreground classes, yielding weighted, mean foreground IoU.

### 3.4. Implementation

The model was implemented in the Python programming language using the Keras interface to Tensorflow Abadi et al. (2016), and trained on one NVIDIA Titan X graphics processing unit (GPU) with 12 GB of memory. For all network architectures, it took roughly 20 minutes to iterate over the entire training set (1 epoch). At test time, the network predicted segmentations at roughly 15 frames per second.

## 4. Results

### 4.1. Segmentation

Weighted foreground IoU was calculated separately for each image, and the median and interquartile range (IQR) of all predictions is reported. As accuracy is not necessarily the same across all clinical planes, the performance of the four networks relative to expert manual segmentation is reported for all views combined, and also for each clinical plane separately (Table 2).

It is instructive to examine intermediate network performance at each successive U-Net (Fig. 6).

- Although Network A contains the most parameters, adding the fine-grained segmentation module increases network performance *at the level of the coarse-grained*

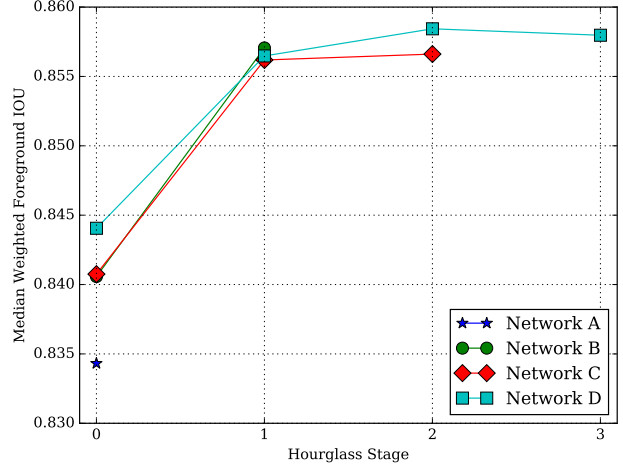


Figure 6: Weighted foreground IoU for architecture and depth.

*U-Net* compared with Network A; i.e., the performance of the coarse-grained segmentation module U-Net (U-Net 0) is  $\approx 0.007$  higher in Networks B and C compared with Network A, and  $\approx 0.003$  higher in Network D compared with Networks B and C.

- There is a substantial increase in performance between the coarse-grained and fine-grained segmentation U-Nets, i.e., U-Nets 0 and 1 ( $\approx 0.016$ ,  $\approx 0.015$ , and  $\approx 0.012$  increases for Networks B, C, and D, respectively).
- In Networks C and D, there is not a substantial increase in performance between successive U-Nets in the fine-grained segmentation module.

As performance is likely to differ between structures, imagewise histograms of foreground IoU are plotted for the best performing network (Network D) for each structure and clinical plane (Fig. 7). In all three clinical planes, performance is worst for the LV myocardium, best in the LV bloodpool, and intermediate in the remaining structures. Relatively poor LV myocardial segmentation performance can be understood intuitively by considering that segmentation error is concentrated primarily at the structure boundaries. Therefore, structures with a high ratio of perimeter-to-area (such as the LV myocardium, which has

Name	View	U-Net 0	U-Net 1	U-Net 2	U-Net 3
Network A	All	0.834 [0.783, 0.871]	—	—	—
	SA	0.843 [0.789, 0.880]	—	—	—
	4C	0.819 [0.765, 0.855]	—	—	—
	2C	0.831 [0.788, 0.863]	—	—	—
Network B	All	0.841 [0.793, 0.876]	0.857 [0.819, 0.885]	—	—
	SA	0.848 [0.800, 0.884]	0.862 [0.820, 0.891]	—	—
	4C	0.831 [0.780, 0.861]	0.845 [0.812, 0.871]	—	—
	2C	0.832 [0.787, 0.864]	0.856 [0.822, 0.882]	—	—
Network C	All	0.841 [0.792, 0.875]	0.856 [0.816, 0.884]	0.857 [0.816, 0.885]	—
	SA	0.849 [0.797, 0.883]	0.862 [0.820, 0.890]	0.862 [0.819, 0.890]	—
	4C	0.830 [0.779, 0.861]	0.843 [0.804, 0.869]	0.844 [0.805, 0.869]	—
	2C	0.830 [0.793, 0.863]	0.855 [0.818, 0.883]	0.857 [0.819, 0.884]	—
Network D	All	0.844 [0.797, 0.877]	0.856 [0.819, 0.884]	0.858 [0.821, 0.886]	0.853 [0.821, 0.886]
	SA	0.851 [0.798, 0.886]	0.862 [0.821, 0.890]	0.863 [0.822, 0.892]	0.863 [0.822, 0.892]
	4C	0.832 [0.781, 0.861]	0.839 [0.805, 0.868]	0.843 [0.811, 0.870]	0.843 [0.811, 0.869]
	2C	0.842 [0.804, 0.869]	0.858 [0.828, 0.884]	0.860 [0.831, 0.886]	0.859 [0.830, 0.886]

Table 2: Network performance with reference to ground truth. Pixel accuracy and weighted foreground IoU of each network are calculated for all views combined and for each view separately. All four networks performed similarly in terms of both metrics. Network performance was highest in the SA view and lowest in the 4C view, though these differences are small.

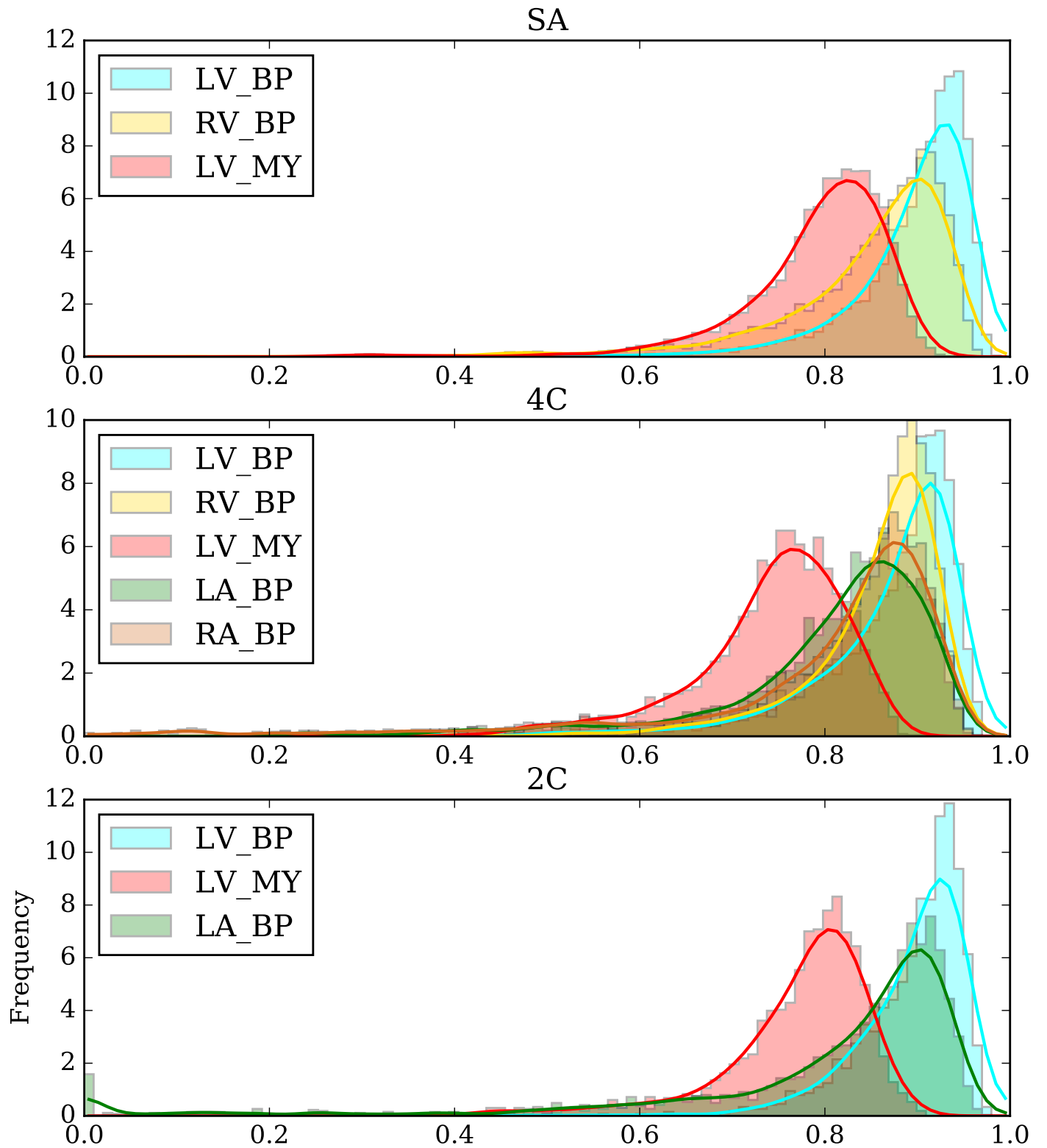


Figure 7: Histograms of IoU for each view and class. Performance relative to expert manual segmentation was highest in the SA view and lowest in the 4C view, though the differences are small.

both an internal and external perimeter, i.e., endocardium and epicardium) are predisposed to perform poorly. A number of factors may contribute to the superior performance of LV bloodpool segmentation.

- The LV myocardium provides a high-contrast boundary along much of the perimeter of the LV bloodpool.
- Compared with other cardiac chambers, the LV bloodpool has relatively less anatomical variation between subjects.
- The three orthogonal planes examined in this study are all defined relative to the left ventricle; therefore, the appearance if the LV is more consistent between subjects.

Representative segmentations produced by Network D in all views are shown for healthy control subjects in Fig. 8 and for patients with overt HCM in Fig. 9. (Note that the ground truth segmentations have been transformed by the predicted parameters rather than the ground truth parameters in order to aid interpretation.) The network successfully transformed the images into the canonical orientation for all cases shown. Notably, the myocardial segmentation consistently excludes papillary muscles and myocardial trabeculation. Moreover, the network appears to reliably identify the atrioventricular valve plane in the long axis views, which is a useful result deserving of attention in future work.

Fig. 10 illustrates the  $\Omega$ -Net behavior on structure detection. Detection rate was defined as the percentage of cases in which weighted foreground IoU exceeded a varying threshold varying from 0.4 to 1.0, plotted on the horizontal axis. The resulting precision-recall curve had an excellent area under the curve (AUC) of 0.992, demonstrating the robustness of the  $\Omega$ -Net’s structure detection.

#### 4.2. Transformation parameters

Ground truth parameters were compared to those predicted by the best performing network (Network D) via correlation, and by Bland Altman plots Fig. 11. It is notable that ground truth transformation parameters (particularly rotation and scale) were not uniformly distributed between views. Nonrandom rotation is to be expected from the fact that the positioning of the patient in the scanner, the protocol for determining imaging planes, the placement of the heart in the chest, and the relationship between imaging planes are all themselves nonrandom; nonrandom scale is likewise to be expected from the variable size of the anatomical structures visible in each view.

Predicted horizontal translation, vertical translation, and rotation parameters were all highly correlated with ground truth ( $R \approx 0.95$ ,  $p < 0.0001$  for all), with the predicted parameters slightly underestimating the ground truth slightly (slope  $\approx 0.87$  for all). No systematic bias was evident on visual inspection of the Bland-Altman plots; 95% of translation errors were within  $\pm 0.07$  (in normalized

image coordinates), and 95% of rotation errors were within  $\pm 0.63$  (in radians). Of the 5% of cases which were outside these bounds, the vast majority were long axis (4C or 2C) views. This is perhaps unsurprising since each patient contributed three SA views, but only two long axis views.

Compared with translation and rotation, correlation between ground truth and predicted scale was slightly lower, though still good ( $R = 0.88$ ,  $p < 0.0001$ ); predicted scale again slightly underestimated ground truth scale ( $s = 0.71\hat{s} + 0.16$ ). There is a marked decrease in network performance above approximately  $\hat{s} = 0.7$ . This may indicate the importance of context information to the network; however, it should be noted that the decrease in performance is accompanied by a sharp decrease in the frequency of cases, and so may also be the result of an insufficient number of samples in the dataset.

#### 4.3. Failure cases

Occasional failure cases were observed, a selection of which are shown in Fig. 12. Each of these failure cases has one or more features which could logically explain the failure. The leftmost column shows an apical SA slice from a severely hypertrophied patient. Patients with such severe disease were relatively uncommon in the dataset, perhaps causing the network to split its attention between the heart and a second “candidate structure” (the cardia of the stomach). The center-left column shows a second apical SA slice from a different subject, where the right ventricle was incorrectly segmented. The signal intensity in this image was low relative to the other patients in the cohort, resulting in a very high contrast image after histogram equalization. The center-right and rightmost columns show long axis views from a patient with a particularly high resolution scan, where the heart occupies the vast majority of the image, with very little context information. In both cases, catastrophic segmentation error follows failure to properly reorient the image into a canonical orientation. However, it should be emphasized that this post hoc reasoning is speculative; we cannot state a definitive causal relationship between these features and the resulting failures.

## 5. Discussion

In this work, we have presented the  $\Omega$ -Net: a novel deep convolutional neural network (CNN) architecture for detection, orientation alignment, and segmentation. We have applied this network to the task of fully automatic whole-heart segmentation and simultaneous transformation into the “canonical” clinical view, which has the potential to greatly simplify downstream analyses of SSFP CMR images. The network was trained end-to-end from scratch to segment five foreground classes (the four cardiac chambers plus the LV myocardium) in three views (SA, 4C, and 2C), without providing prior knowledge of the view being segmented. The dataset was highly heterogeneous from the standpoint of anatomical variation,

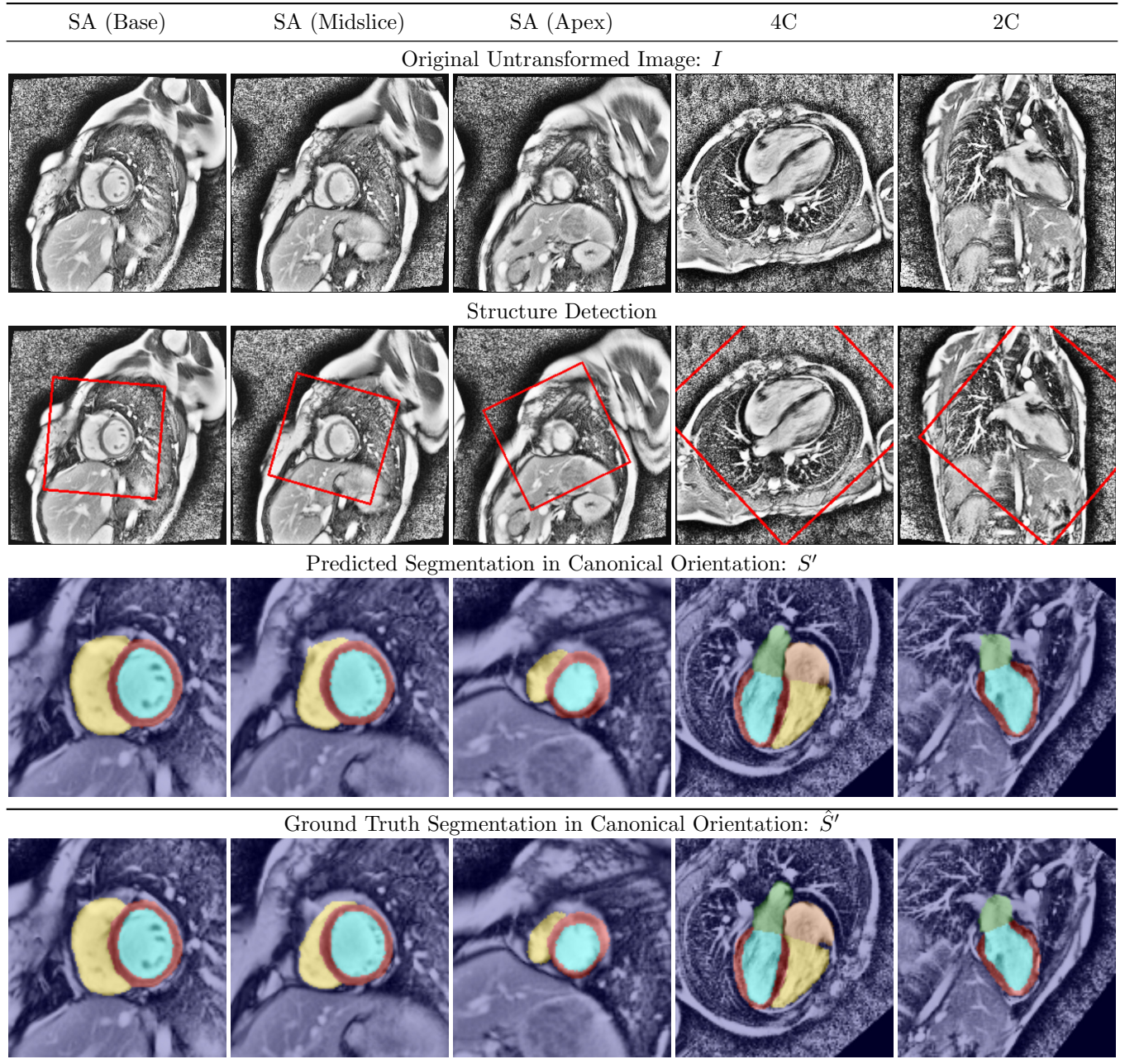


Figure 8: Representative segmentation results in healthy control subjects. See text for discussion.

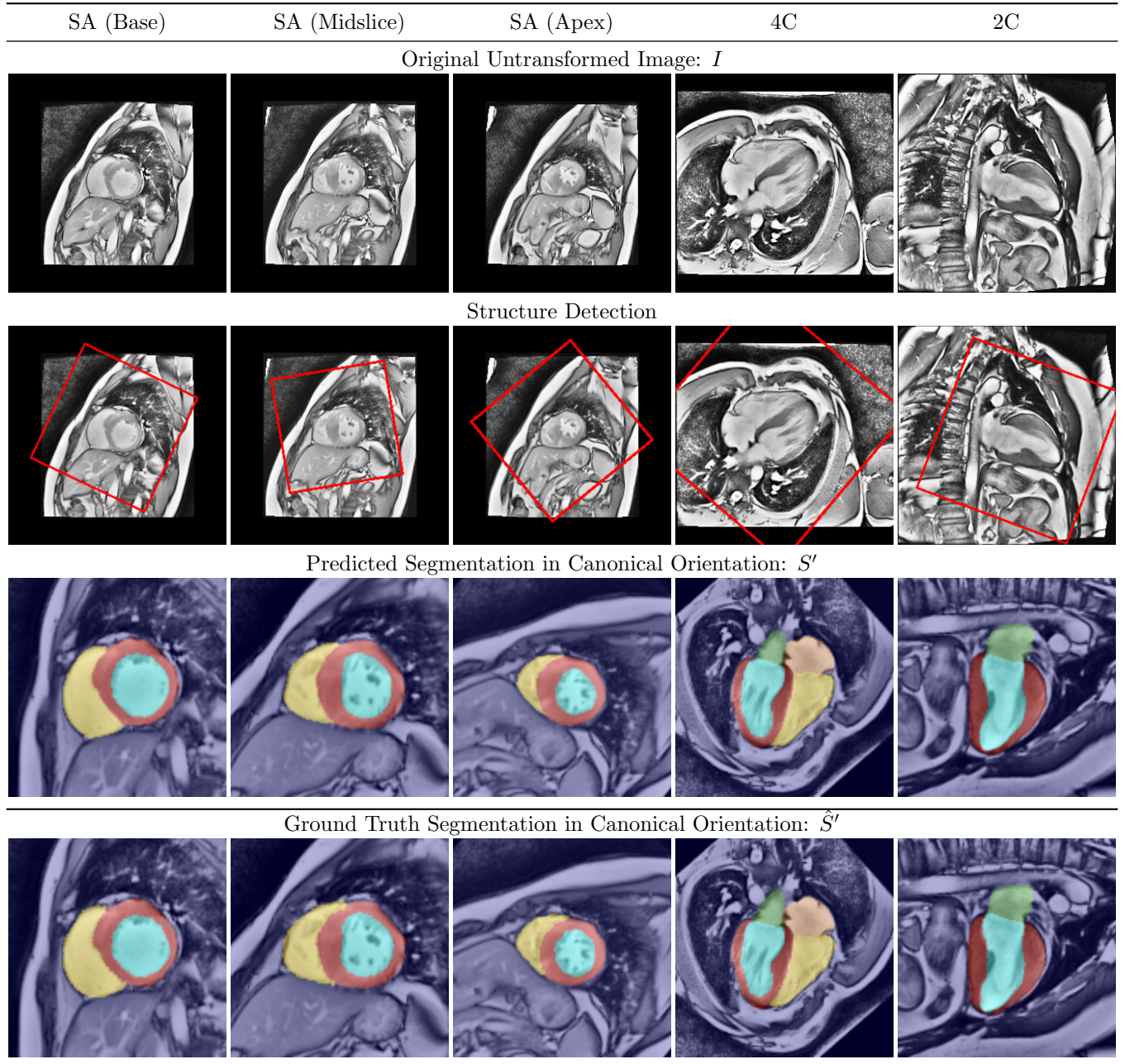


Figure 9: Representative segmentation results in patients with overt HCM. See text for discussion.

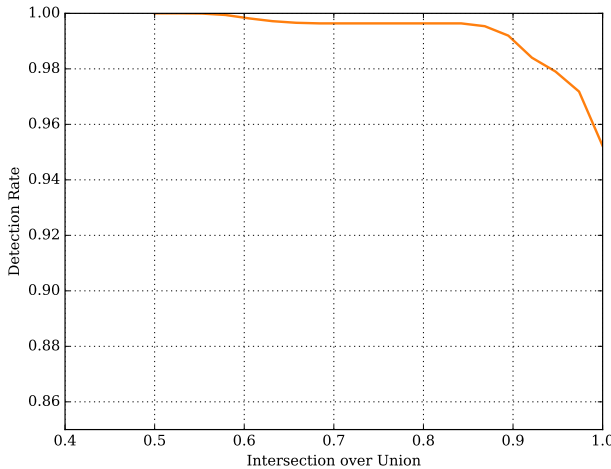


Figure 10: Precision-Recall curve.

including both healthy subjects and patients with overt hypertrophic cardiomyopathy. Data was acquired from both 1.5-T and 3-T magnets as part of a multicenter trial involving 10 institutions. In cross-validation experiments, the network performed well in predicting both the parameters of the transformation, and the cardiac segmentation.

The work is novel in three principal ways. First, this network predicts five foreground classes in three clinical views, which is a substantially more difficult problem than has been addressed previously in the literature Vigneault et al. (2017). Second, a spatial transformer network module Jaderberg et al. (2015) was used to rotate each view into a canonical orientation, simplifying the task of both the downstream network and the physician interpreting the images. Third, the proposed architecture takes loose inspiration from the cascaded classifier models proposed by Viola and Jones (2001), in that U-Net 0 performs coarse-grained segmentation (in order to predict transformation parameters), and the transformed image is then provided as input to a fine-grained segmentation module (U-Nets 1, 2, and 3).

While the dataset was manually augmented by transforming the input with small, rigid, affine transformations, it is worth noting that data augmentation is performed *implicitly* in the fine segmentation module by virtue of the fact that, in the early stages of training, the transformation parameters predicted by the attention module are random.

Although the dataset included three orthogonal cardiac planes and both healthy and disease subjects, the dataset on which the  $\Omega$ -Net was trained is nonetheless subject to certain limitations. First, other cardiac planes used in clinical practice (such as the axial, three-chamber, and RV long axis views) should be added in future work. It has been demonstrated in this work that the technique is robust to variation (primarily in LV structure) due to overt HCM. However, the trained model would *not* be expected

to generalize to unrelated pathologies such as tetralogy of Fallot, pulmonary hypertension, or arrhythmogenic right ventricular cardiomyopathy, without fine-tuning or (ideally) training from scratch on an expanded dataset. It would also be useful and interesting to test this on other CMR pulse sequences (such as gradient echo) and on additional modalities (i.e., cardiac computed tomography and echocardiography). It could also be interesting to apply this technique to other areas within biomedical image segmentation where detection, reorientation, and segmentation are useful, such as in fetal imaging.

A variety of opportunities present themselves in terms of optimizing the  $\Omega$ -Net architecture. For example, the network was trained to segment individual image frames, without spatial or temporal context; modifying the architecture to allow information sharing between temporal frames and spatial slices has the potential to increase accuracy and consistency. The E-Net (“Efficient Net”) provides modifications to the U-Net blocks which increase computational and memory efficiency, while preserving accuracy (Paszke et al., 2016); these lessons have been applied successfully to cardiac segmentation (Lieman-Sifry et al., 2017), and could theoretically be applied here as well.

## 6. Summary

Here, we have presented  $\Omega$ -Net (Omega-Net): a novel CNN architecture for simultaneous detection, transformation into a canonical orientation, and semantic segmentation. First, a coarse-grained segmentation is performed on the input image; second, the features learned during this coarse-grained segmentation are used to predict the parameters needed to transform the input image into a canonical orientation; and third, a fine-grained segmentation is performed on the transformed image. The network was trained end-to-end from scratch to predict five foreground classes in three clinical views, constituting a substantially more challenging problem compared with prior work. The trained network performed well in a cohort of both healthy subjects and patients with severe LV pathology. We believe this architecture represents a substantive advancement over prior approaches, with implications for biomedical image segmentation more generally.

## Acknowledgements

D.M. Vigneault is supported by the NIH-Oxford Scholars Program and the NIH Intramural Research Program. W. Xie is supported by the Google DeepMind Scholarship, and the EPSRC Programme Grant Seebibyte EP/M013774/1.

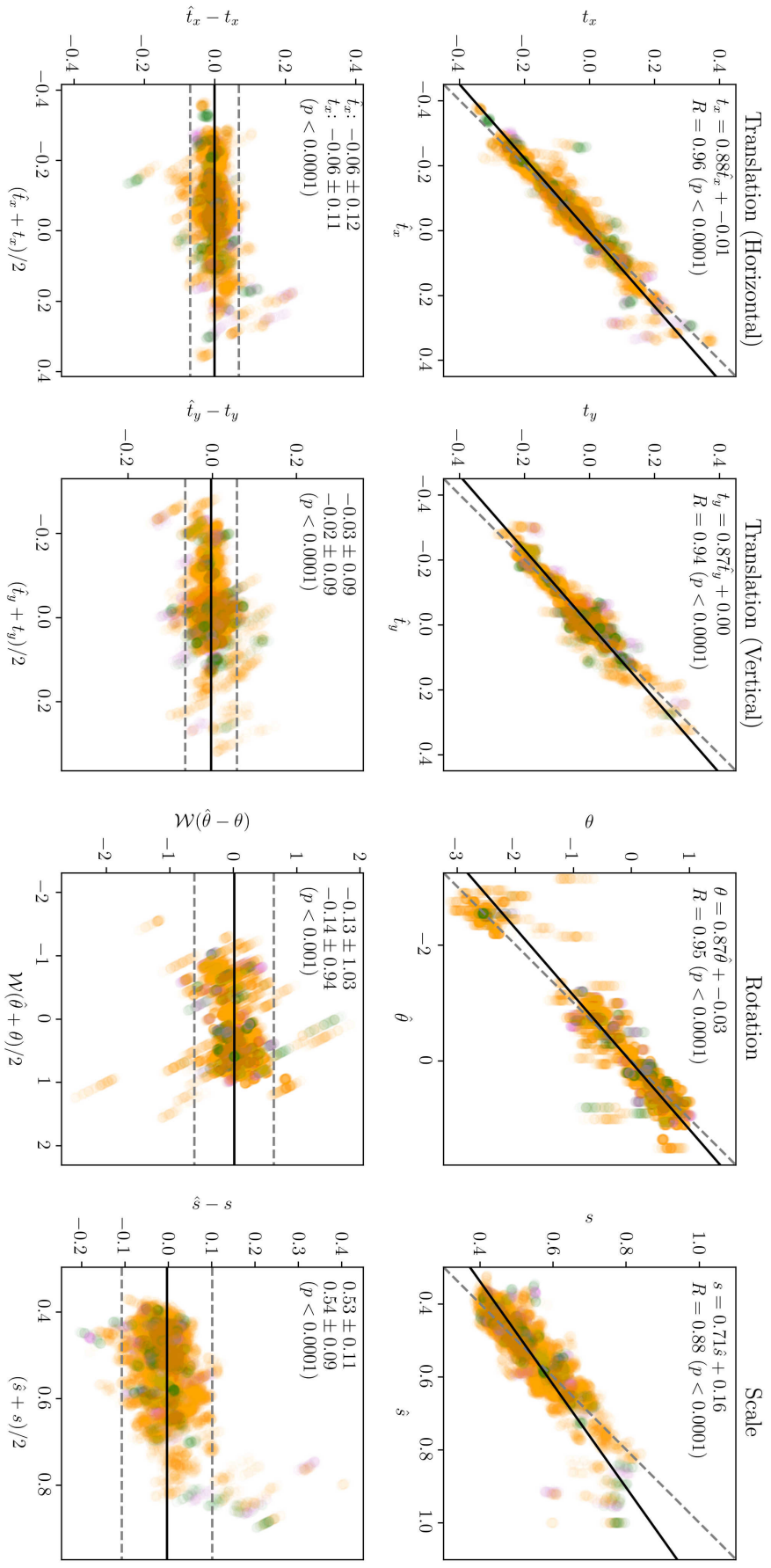


Figure 11: Transformation errors. Correlation (top) and Bland-Altman (bottom) plots comparing predicted and ground truth transformation parameters. SA, 4C, and 2C errors are represented by orange, green, and purple points, respectively (points have been rendered partially translucent to aid interpretation of densely occupied regions). In the correlation plots, the best-fit trendline is represented as a solid black line, and the ideal trendline ( $y = x$ ) is represented as a dashed gray line. The equation of the trendline and the Pearson correlation coefficient  $R$  are also given. In the Bland-Altman plots, the mean difference is represented as a solid black horizontal line, and the limits  $\pm 1.96$  standard deviations are represented as a dashed gray horizontal line.

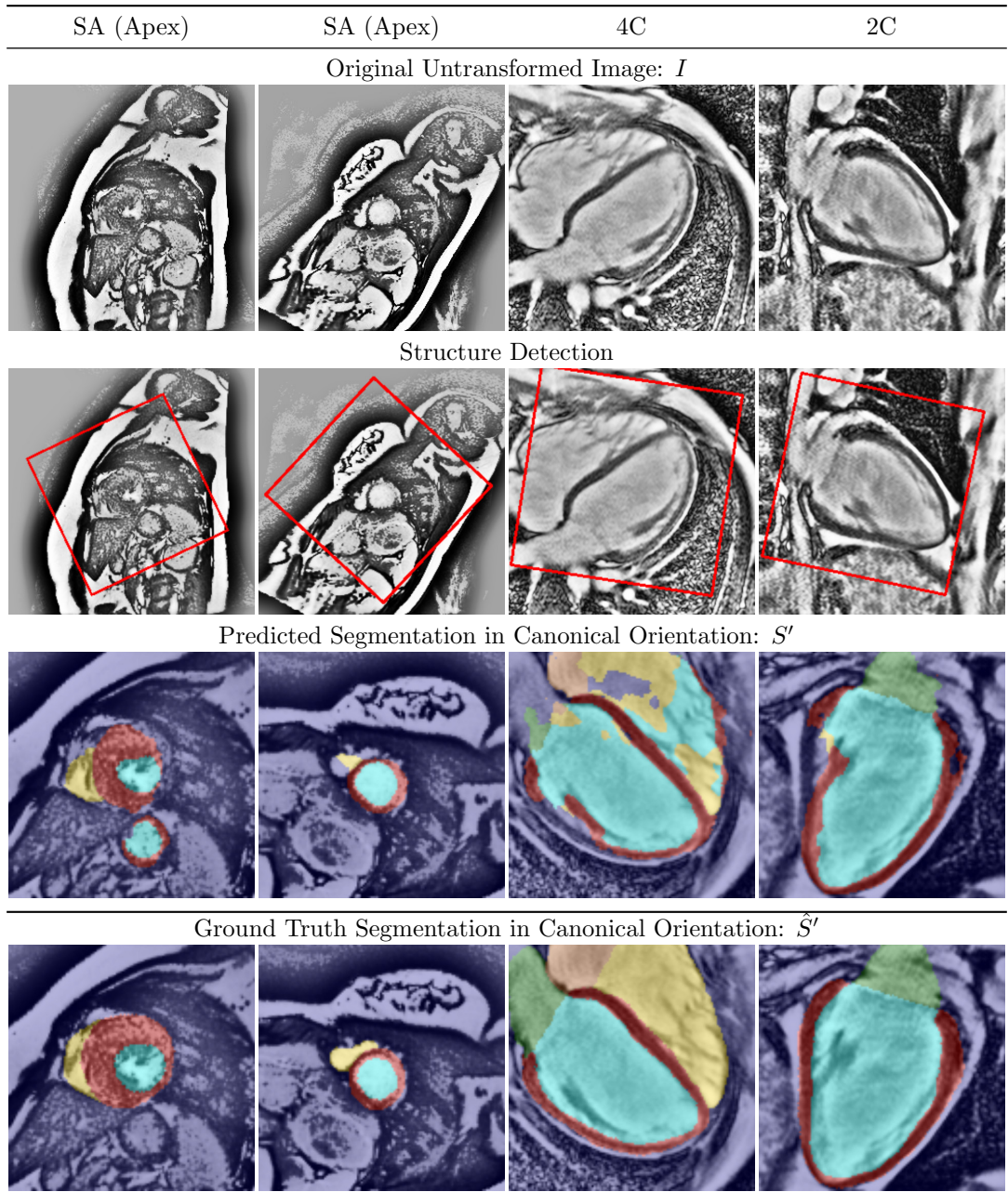


Figure 12: Selected failure cases from CNN segmentation. See text for discussion.

## References

## References

Abadi M, Barham P, Chen J, Chen Z, Davis A, Dean J, Devin M, Ghemawat S, Irving G, Isard M, Kudlur M, Levenberg J, Monga R, Moore S, Murray DG, Steiner B, Tucker P, Vasudevan V, Warden P, Wicke M, Yu Y, Zheng X. TensorFlow: A system for large-scale machine learning; 2016. URL: <https://arxiv.org/pdf/1605.08695.pdf>. arXiv:arXiv:1605.08695v2.

He K, Zhang X, Ren S, Sun J. Deep Residual Learning for Image Recognition. In: CVPR. 2016. arXiv:arXiv:1512.03385v1.

Ioffe S, Szegedy C. Batch Normalization: Accelerating Deep Network Training by Reducing Internal Covariate Shift. In: ICML. volume 37; 2015. p. 81–7. URL: <http://arxiv.org/abs/1502.03167>. doi:10.1007/s13398-014-0173-7\_2. arXiv:arXiv:1011.1669v3.

Jaderberg M, Simonyan K, Zisserman A, Kavukcuoglu K. Spatial Transformer Networks. In: NIPS. 2015. p. 1–14. doi:10.1038/nbt.3343. arXiv:arXiv:1506.02025v1.

Kingma D, Ba J. Adam: A Method for Stochastic Optimization. In: ICLR. 2015. arXiv:arXiv:1412.6980v9.

Krizhevsky A, Sutskever I, Hinton GE. ImageNet Classification with Deep Convolutional Neural Networks. In: NIPS. 2012. .

Lieman-Sifry J, Le M, Lau F, Sall S, Golden D. FastVentricle: Cardiac Segmentation with ENet. In: FIMH. 2017. URL: <http://arxiv.org/abs/1704.04296>. arXiv:1704.04296.

Long J, Shelhamer E, Darrell T. Fully convolutional networks for semantic segmentation. In: CVPR. volume 07-12-June; 2015. p. 3431–40. doi:10.1109/CVPR.2015.7298965. arXiv:1411.4038.

Luo G, An R, Wang K, Dong S, Zhang H. A Deep Learning Network for Right Ventricle Segmentation in Short-Axis MRI. Computing in Cardiology 2016;43:485–8.

Newell A, Yang K, Deng J. Stacked Hourglass Networks for Human Pose Estimation. In: ECCV. 2016. URL: <http://arxiv.org/abs/1603.06937>. doi:10.1007/978-3-319-46484-8. arXiv:1603.06937.

Noh H, Hong S, Han B. Learning Deconvolution Network for Semantic Segmentation. In: ICCV. volume 1; 2015. URL: <http://arxiv.org/abs/1505.04366>. doi:10.1109/ICCV.2015.178. arXiv:1505.04366.

Paszke A, Chaurasia A, Kim S, Culurciello E. ENet: A Deep Neural Network Architecture for Real-Time Semantic Segmentation. 2016. URL: <https://arxiv.org/abs/1606.02147>. arXiv:arXiv:1606.02147v1.

Peng P, Lekadir K, Gooya A, Shao L, Petersen SE, Frangi AF. A review of heart chamber segmentation for structural and functional analysis using cardiac magnetic resonance imaging. MAGMA 2016;29(2):155–95. doi:10.1007/s10334-015-0521-4.

Poudel RP, Lamata P, Montana G. Recurrent Fully Convolutional Neural Networks for Multi-slice MRI Cardiac Segmentation. In: HVSMR. 2016. URL: <http://arxiv.org/abs/1608.03974>. doi:10.1007/978-3-319-52280-7\_8. arXiv:1608.03974.

Ronneberger O, Fischer P, Brox T. U-Net: Convolutional Networks for Biomedical Image Segmentation. In: MICCAI. 2015. p. 234–41. doi:10.1007/978-3-319-24574-4\_28. arXiv:1505.04597.

Saxe AM, McClelland JL, Ganguli S. Exact solutions to the non-linear dynamics of learning in deep linear neural networks. In: ICLR. 2014. p. 1–22. URL: <http://arxiv.org/abs/1312.6120>. arXiv:1312.6120.

Simonyan K, Zisserman A. Very Deep Convolutional Networks for Large-Scale Image Recognition. In: ICLR. 2014. p. 1–14. arXiv:arXiv:1409.1556v6.

Tan LK, Liew YM, Lim E, McLaughlin RA. Cardiac Left Ventricle Segmentation using Convolutional Neural Network Regression. In: IECBES. 2016. p. 490–3.

Tan LK, Liew YM, Lim E, McLaughlin RA. Convolutional neural network regression for short-axis left ventricle segmentation in cardiac cine MR sequences. Medical Image Analysis 2017;39:78–86. URL: <https://www.sciencedirect.com/science/article/pii/S1361841517300543>. doi:10.1016/j.media.2017.04.002.

Tran PV. A Fully Convolutional Neural Network for Cardiac Segmentation in Short-Axis MRI; 2016. URL: <http://arxiv.org/abs/1604.00494>. arXiv:1604.00494.

Vigneault DM, Pourmorteza A, Bluemke DA, Noble JA. Quantifying Cardiac Function from Computed Tomography via Multiresolution Loop Subdivision Surface Registration with Automatically-Generated Meshes. Medical Image Analysis [Under Review] 2017;.

Viola P, Jones M. Rapid Object Detection using a Boosted Cascade of Simple Features. In: CVPR. 2001. .

Xie W, Noble JA, Zisserman A. Microscopy Cell Counting with Fully Convolutional Regression Networks. In: MICCAI Workshop. 2015. p. 1–10. URL: <http://www.tandfonline.com/myaccess.library.utoronto.ca/doi/full/10.1080/21681163.2016.1149104>. doi:10.1080/21681163.2016.1149104.

Yu F, Koltun V. Multi-Scale Context Aggregation by Dilated Convolutions. In: ICLR. 2016. p. 1–9. URL: <http://arxiv.org/abs/1511.07122>. doi:10.16373/j.cnki.ahr.150049. arXiv:1511.07122.